



# Flame simulations with an open-source code<sup>☆</sup>

Adhiraj Dasgupta<sup>a,\*</sup>, Esteban Gonzalez-Juez<sup>a</sup>, Daniel C. Haworth<sup>b</sup>

<sup>a</sup> Combustion Science & Engineering, Inc., 8940 Old Annapolis Road, Suite L, Columbia, MD 21045, USA

<sup>b</sup> Research Building East, Department of Mechanical and Nuclear Engineering, The Pennsylvania State University, University Park, PA 16802, USA

## ARTICLE INFO

### Article history:

Received 10 July 2018

Received in revised form 29 October 2018

Accepted 12 November 2018

Available online 28 November 2018

### Keywords:

Combustion

Turbulent combustion

CFD

Large-Eddy Simulation

OpenFOAM<sup>®</sup>

Mixture-averaged transport

## ABSTRACT

Flame simulations are used to gain insight into combustion physics and to design combustion systems such as piston engines, gas-turbine engines, and process heaters. In these simulations, the balance between reaction and molecular mixing plays a key role. To model molecular mixing, using a full multicomponent approach leads to high accuracy at the expense of a hefty computational cost. Thus, the use of a mixture-averaged model is usually preferred. Hence, this paper presents and tests a new OpenFOAM<sup>®</sup>-based code that incorporates a detailed, mixture-averaged approach for calculating transport properties in reacting flows, and provides a capability to solve either fully-compressible or low-Mach-number governing equations. The code is made readily available on GitHub and is written completely in OpenFOAM<sup>®</sup>'s native code framework, making it highly portable and easy to maintain, enhance, and extend. It is tested by modeling two laminar flames, and two turbulent flames undergoing extinction and reignition. Overall, predictions with the present code are seen to be in good agreement with experimental and direct-numerical-simulation data.

### Program Summary

**Program Title:** laminarReactingFoam & laminarReactingLMFoam

**Program Files doi:** <http://dx.doi.org/10.17632/h8hch3hs9p.1>

**Licensing provisions:** GPLv3

**Programming language:** C++.

**Nature of problem:** In high-resolution flame simulations it is important to calculate the transport properties without using simplified models in order to capture the physics of the problem. Assumptions such as unity Lewis number do not always provide an accurate answer, and in some cases may not be able to capture some of the relevant physics.

**Solution method:** The present code adds the functionality to calculate the transport properties of the gas mixture using a detailed, mixture-averaged formulation.

© 2018 Elsevier B.V. All rights reserved.

## 1. Introduction

Flame simulations have provided valuable insight into combustion physics [1] and facilitated the enhancement of the design of combustion systems such as internal-combustion engines [2], gas-turbine engines [3], process heaters, and furnaces. Many combustion codes have been used for this purpose [4–11]. Most of them are not readily available. Thus, several open-source codes have been developed. Among these, perhaps the most popular ones are those from the open-source library OpenFOAM<sup>®</sup> [12,13], notably its main reacting code: reactingFoam. Some authors have implemented flamelet-based models within OpenFOAM<sup>®</sup>'s code

framework in order to model turbulent flames, in particular to account for turbulence-chemistry interactions [14,15].

OpenFOAM<sup>®</sup>'s reacting codes use a highly simplified molecular-transport model, which is discussed later. This model could be justified in some simulations of strongly-turbulent flames where molecular-mixing phenomena, e.g., differential diffusion, are considered to be not of leading-order importance. Such cases could include, for example, Reynolds-Average Simulations (RAS) where eddy viscosities and diffusivities are much larger than molecular viscosities and diffusivities, or in Large-Eddy Simulations (LES) where subgrid-scale (SGS) viscosities and diffusivities are significantly larger than their molecular counterparts. As a result, this simplified molecular-transport modeling is acceptable in many practical simulations. In fact, reactingFoam and its derivatives have been used successfully in various combustion studies [13,16–23].

This simplified molecular-mixing approach, however, is difficult to justify in the simulation of laminar flames intended to provide physical insight or tabulated information for flamelet

<sup>☆</sup> This paper and its associated computer program are available via the Computer Physics Communication homepage on ScienceDirect (<http://www.sciencedirect.com/science/journal/00104655>).

\* Corresponding author.

E-mail address: [adasgupta@csefire.com](mailto:adasgupta@csefire.com) (A. Dasgupta).

turbulent-combustion models [24–26]. It is also hard to justify in LES when values of SGS viscosities and diffusivities are comparable to their molecular counterparts. Moreover, this simplified modeling cannot be justified when an attempt is made to resolve all physical scales, within continuum mechanics, with Direct Numerical Simulations (DNS) in order to provide new physical insight.

To extend the capability of OpenFOAM® to simulate these cases, the present work describes and tests a new OpenFOAM®-based code that calculates molecular transport using a realistic, mixture-averaged approach (Section 2) and removes related simplifying assumptions. This work differs from similar OpenFOAM®-based implementations [27,28] in four important ways. First, the code is being made readily available [29]. Second, it is thoroughly validated for both laminar and turbulent flames by considering the following tests: a one-dimensional, laminar, premixed, methane–air flame (Section 3.1); a two-dimensional, laminar, non-premixed, methane–air flame (Section 3.2); and two three-dimensional, turbulent, non-premixed, syngas flames undergoing extinction and reignition (Sections 3.3.1 and 3.3.2). Regarding these turbulent-flame tests, it is important to note that extinction and reignition are difficult to model [30]. Third, the present work includes the option to switch from a fully compressible form of the governing equations to a low-Mach-number form. Last, the code is written completely in OpenFOAM®'s native code framework, a feature which should make it highly portable and easy to use, maintain, enhance, and extend.

## 2. Numerical model

The governing equations for a fully compressible reacting flow are:

$$\frac{\partial \rho}{\partial t} + \frac{\partial(\rho u_i)}{\partial x_i} = 0, \quad (1)$$

$$\frac{\partial \rho u_i}{\partial t} + \frac{\partial(\rho u_j u_i)}{\partial x_j} = -\frac{\partial p}{\partial x_i} + \frac{\partial \tau_{ij}}{\partial x_j} + \rho f_i, \quad (2)$$

$$\frac{\partial \rho Y_k}{\partial t} + \frac{\partial(\rho u_j Y_k)}{\partial x_j} = -\frac{\partial J_{k,j}}{\partial x_j} + \dot{\omega}_k, \quad (3)$$

$$\begin{aligned} \frac{\partial \rho h_s}{\partial t} + \frac{\partial(\rho u_j h_s)}{\partial x_j} + \frac{\partial \rho K}{\partial t} + \frac{\partial(\rho u_j K)}{\partial x_j} = & -\frac{\partial q_j}{\partial x_j} + \frac{\partial p}{\partial t} + \rho u_j f_i + q_{rad} \\ & - \sum_{l=1}^N \dot{\omega}_l \Delta h_{f,l}^\circ + \frac{\partial(\tau_{ij} u_i)}{\partial x_j}, \end{aligned} \quad (4)$$

$$p = \rho R_u T \sum_{l=1}^N \frac{Y_l}{W_l}. \quad (5)$$

Here  $\rho$  is density,  $u_i$  is velocity,  $p$  is pressure,  $\tau_{ij}$  is the viscous stress tensor,  $Y_k$  is the mass fraction of species  $k$ ,  $J_{k,j}$  is the molecular diffusion flux of the  $k$ th species,  $\dot{\omega}_k$  is the production rate of species  $k$ ,  $h_s$  is the mixture sensible enthalpy,  $K$  is the kinetic energy per unit mass of the flow,  $q_i$  is the heat flux,  $f_i$  is the body force per unit volume (e.g., due to gravity),  $q_{rad}$  is the radiative heat source,  $\Delta h_{f,k}^\circ$  is the standard state heat of formation of species  $k$ ,  $R_u$  is the universal gas constant, and  $W_k$  is the molecular weight of species  $k$ . Unless stated otherwise, radiation and body forces are neglected in this work.

Of particular interest is the energy equation for the fully compressible formulation. The term  $\frac{\partial p}{\partial t}$  in Eq. (4) drives acoustic waves in the system and can lead to an unstable simulation. To deal with this, a low-Mach-number formulation is often used in combustion applications. With this approximation [31], the pressure is split into two parts as  $p = p_0 + p_d$ . Here  $p_0$  is the thermodynamic pressure (which is uniform), and the hydrodynamic pressure  $p_d$

drives the flow field. Under the low-Mach-number approximation, the governing equations are Eqs. (1), (3), and

$$\frac{\partial \rho u_i}{\partial t} + \frac{\partial(\rho u_j u_i)}{\partial x_j} = -\frac{\partial p_d}{\partial x_i} + \frac{\partial \tau_{ij}}{\partial x_j} + \rho f_i, \quad (6)$$

$$\frac{\partial \rho h_s}{\partial t} + \frac{\partial(\rho u_j h_s)}{\partial x_j} = -\frac{\partial q_j}{\partial x_j} + q_{rad} - \sum_{l=1}^N \dot{\omega}_l \Delta h_{f,l}^\circ, \quad (7)$$

$$p_0 = \rho R_u T \sum_{l=1}^N \frac{Y_l}{W_l}. \quad (8)$$

Due to the low-Mach-number assumption, the unsteady term  $\frac{\partial p}{\partial t}$  is dropped from Eq. (7), as are the contributions from the mean flow kinetic energy  $\left[ \frac{\partial \rho K}{\partial t} + \frac{\partial(\rho u_j K)}{\partial x_j} \right]$ , and the viscous stress term  $\frac{\partial(\tau_{ij} u_i)}{\partial x_j}$ . As a result of ignoring the pressure term, acoustic waves are automatically eliminated from the simulation. When resolving such waves is not needed, as in the present tests, low-Mach-number simulations can significantly reduce the computational cost in some cases, as indicated later. If in addition the thermodynamic pressure is also steady then density changes in the flow are due to temperature change and mixing.

For ideal gases, the standard-state thermodynamic properties are functions of temperature only. The thermodynamic properties are evaluated as

$$\frac{C_{p,k}}{R_u} = \sum_{n=0}^4 a_{n,k} T^n,$$

$$\frac{H_k}{R_u T} = \sum_{n=0}^4 \frac{a_{n,k} T^n}{n+1} + \frac{a_{n,5}}{T},$$

where  $T$  is temperature,  $C_{p,k}$  is the molar specific heat at constant pressure for species  $k$ , and  $H_k$  is the molar enthalpy. The coefficients  $a_{n,k}$  are those from the well-known NASA polynomials [32]. To calculate the chemical source terms  $\dot{\omega}_k$  in Eqs. (3), (4), and (7), OpenFOAM®'s native implementation of the operator-splitting method was used, together with its extrapolation-based stiff ODE solver SIBS [33].

Closure for molecular mixing is the main contribution of the present work. Mass diffusion is modeled in this work using the Hirschfelder and Curtiss approximation [34] and using a correction velocity approach to ensure mass conservation [35,36]. The diffusion flux for species  $k$  is modeled as

$$J_{k,i} = \rho \left( -D_k \frac{\partial X_k}{\partial x_i} + Y_k V_i^c \right),$$

where  $X_k$  is the mole fraction of species  $k$ ,  $D_k$  is the mixture-averaged diffusivity for species  $k$ , and  $V_i^c$  is a spatially-varying correction velocity, which is the same for all species. The heat flux is given by

$$q_i = -\lambda \frac{\partial T}{\partial x_i} + \sum_{l=1}^N h_l J_{l,i},$$

where  $\lambda$  is the thermal conductivity of the gas mixture, and  $h_l$  is the specific enthalpy of species  $l$ . Lastly, the viscous stress tensor  $\tau_{ij}$  is computed as

$$\tau_{ij} = 2\mu S_{ij} - \frac{2}{3}\mu S_{kk}\delta_{ij},$$

where  $\mu$  is the dynamic viscosity, and

$$S_{ij} = \frac{1}{2} \left( \frac{\partial u_i}{\partial x_j} + \frac{\partial u_j}{\partial x_i} \right)$$

is the strain rate tensor.

The viscosity of the gas-phase species  $k$  is given by [34,35]

$$\mu_k = \frac{5}{16} \frac{\sqrt{\pi m_k k_B T}}{\pi \sigma_k^2 \Omega^{(2,2)*}}, \quad (9)$$

where  $\sigma_k$  is the Lennard-Jones collision diameter,  $m_k$  is the molecular mass for species  $k$ ,  $k_B$  is Boltzmann's constant, and  $\Omega^{(2,2)*}$  is the reduced collision integral, which is a function of the reduced temperature  $T_k^*$  given by

$$T_k^* = \frac{k_B T}{\varepsilon_k},$$

where  $\varepsilon_k$  is the Lennard-Jones potential well depth for species  $k$ . The collision integrals are evaluated from curve-fits to the reduced temperature [37].

The binary diffusion coefficient for gas-phase species  $j$  and  $k$  is given by [34,35]

$$D_{jk} = \frac{3}{16} \frac{\sqrt{2\pi k_B^3 T^3 / m_{jk}}}{p \pi \sigma_{jk}^2 \Omega^{(1,1)*}}, \quad (10)$$

where  $m_{jk}$  is the reduced molecular mass for species  $j$  and  $k$ , defined as

$$m_{jk} = \frac{m_j m_k}{m_j + m_k},$$

$\sigma_{jk}$  is the reduced collision diameter, and the reduced collision integral  $\Omega^{(1,1)*}$  is a function of the reduced temperature  $T_{jk}^*$ . These parameters are calculated based on whether the two molecules involved are both polar, both non-polar or one polar and the other non polar.

For the case of two non-polar molecules or two polar molecules interacting, the reduced quantities are defined as

$$\frac{\varepsilon_{jk}}{k_B} = \sqrt{\left(\frac{\varepsilon_j}{k_B}\right) \left(\frac{\varepsilon_k}{k_B}\right)},$$

$$\sigma_{jk} = \frac{1}{2} (\sigma_j + \sigma_k).$$

For a non-polar molecule interacting with a polar one, the reduced polarizability  $\alpha_n^*$  and the reduced dipole moment  $\mu_p^*$  are defined as

$$\alpha_n^* = \frac{\alpha_n}{\sigma_n^3},$$

$$\mu_p^* = \frac{\mu_p}{\sqrt{\varepsilon_p \sigma_p^3}},$$

where  $\alpha$  denotes the polarizability and  $\mu$  denotes the dipole moment; the subscript  $p$  refers to the polar species and the subscript  $n$  to the non-polar species. The reduced temperature  $T_{jk}^*$  is defined as

$$T_{jk}^* = \frac{k_B T}{\varepsilon_{jk}}.$$

The reduced quantities are calculated as

$$\frac{\varepsilon_{np}}{k_B} = \zeta^2 \sqrt{\left(\frac{\varepsilon_n}{k_B}\right) \left(\frac{\varepsilon_p}{k_B}\right)},$$

$$\sigma_{np} = \frac{1}{2} (\sigma_n + \sigma_p) \zeta^{-\frac{1}{6}},$$

where

$$\zeta = 1 + \frac{1}{4} \alpha_n^* \mu_p^* \sqrt{\frac{\varepsilon_p}{\varepsilon_n}}.$$

The thermal conductivity is assumed to have contributions from translational, rotational, and vibrational components. The thermal

conductivity of species  $k$  is given by [35,38]

$$\lambda_k = \frac{\mu_k}{W_k} (f_{trans,k} C_{vk,trans} + f_{rot,k} C_{vk,rot} + f_{vib,k} C_{vk,vib}), \quad (11)$$

where  $C_{vk,trans}$ ,  $C_{vk,rot}$ , and  $C_{vk,vib}$  are respectively the translational, rotational, and vibrational contributions to the constant-volume specific heat  $C_{vk}$  of species  $k$ ,

$$f_{trans,k} = \frac{5}{2} \left( 1 - \frac{2}{\pi} \frac{C_{vk,rot}}{C_{vk,trans}} \frac{A_k}{B_k} \right),$$

$$f_{rot,k} = \frac{\rho_k D_{kk}}{\mu_k} \left( 1 + \frac{2}{\pi} \frac{A_k}{B_k} \right),$$

$$f_{vib,k} = \frac{\rho_k D_{kk}}{\mu_k}.$$

Here the self-diffusion coefficient  $D_{kk}$  is obtained by substituting  $j = k$  in Eq. (10), and the density of gas-phase species  $k$  is obtained as

$$\rho_k = \frac{p W_k}{R_u T}.$$

Further,

$$A_k = \frac{5}{2} - \frac{\rho_k D_{kk}}{\mu_k},$$

$$B_k = Z_{rot,k} + \frac{2}{\pi} \left( \frac{5}{3} \frac{C_{vk,rot}}{R_u} + \frac{\rho_k D_{kk}}{\mu_k} \right).$$

Here  $Z_{rot,k}$  is the rotational relaxation number for species  $k$  and is given by

$$Z_{rot,k}(T) = Z_{rot,k}(298) \frac{F_k(298)}{F_k(T)},$$

where

$$F_k(T) = 1 + \frac{\pi^{\frac{3}{2}}}{2} \left( \frac{\varepsilon_k/k_B}{T} \right)^{\frac{1}{2}} + \left( \frac{\pi^2}{4} + 2 \right) \left( \frac{\varepsilon_k/k_B}{T} \right) + \pi^{\frac{3}{2}} \left( \frac{\varepsilon_k/k_B}{T} \right).$$

The translational and rotational components of the gas specific heat are dependent on the kind of molecule under consideration. For a linear molecule,

$$\frac{C_{vk,trans}}{R_u} = \frac{3}{2},$$

$$\frac{C_{vk,rot}}{R_u} = 1,$$

$$C_{vk,vib} = C_{vk} - \frac{5}{2} R_u.$$

For a non-linear molecule

$$\frac{C_{vk,trans}}{R_u} = \frac{3}{2},$$

$$\frac{C_{vk,rot}}{R_u} = \frac{3}{2},$$

$$C_{vk,vib} = C_{vk} - 3 R_u.$$

For a single atom (for example H, O, etc.) there are no internal contributions to the specific heat. Hence

$$\frac{C_{vk,trans}}{R_u} = \frac{3}{2},$$

$$\frac{C_{vk,rot}}{R_u} = 0,$$

$$C_{vk,vib} = 0.$$

Transport properties for the mixture are computed using a mixture-averaged approach. The mixture-averaged diffusivities

are obtained as [35,39]

$$D_k = \frac{1 - Y_k}{\sum_{l=1}^N \frac{X_l}{D_{kl}}}, \quad (12)$$

where  $D_{kl}$  is the binary diffusivity for the species pair  $k$  and  $l$ . The mixture viscosity is obtained as [35,40]

$$\mu = \sum_{l=1}^N \frac{X_l \mu_l}{\sum_{j=1}^N X_j \Phi_{lj}}, \quad (13)$$

where  $\mu_l$  is the dynamic viscosity of species  $l$ , and

$$\Phi_{mn} = \frac{1}{\sqrt{8}} \left( 1 + \frac{W_m}{W_n} \right)^{-\frac{1}{2}} \left[ 1 + \left( \frac{\mu_m}{\mu_n} \right)^{\frac{1}{2}} \left( \frac{W_n}{W_m} \right)^{\frac{1}{4}} \right]^2. \quad (14)$$

The mixture-averaged thermal conductivity is obtained as [35,41]

$$\lambda = \frac{1}{2} \left( \sum_{l=1}^N X_l \lambda_l + \frac{1}{\sum_{l=1}^N X_l / \lambda_l} \right), \quad (15)$$

where  $\lambda_l$  is the thermal conductivity of species  $l$ . To speed up calculations, the temperature-dependent parts of the transport properties for the individual species are fitted using the method of least squares implemented in the GNU Scientific Library [42]. The logarithms of the properties are fitted to polynomials in the logarithm of temperature. Details of the implementation have also been reported elsewhere [43].

In contrast, reactingFoam models molecular mixing with the following simplified model:

$$\begin{aligned} J_{k,i} &= -\rho \alpha_{N_2} \frac{\partial Y_k}{\partial x_i}, \\ q_i &= -\rho \alpha_{N_2} \frac{\partial h_s}{\partial x_i}, \\ \tau_{ij} &= 2\mu_{N_2} S_{ij} - \frac{2}{3} \mu_{N_2} S_{kk} \delta_{ij}, \end{aligned}$$

where  $\mu_{N_2}$ , and  $\alpha_{N_2}$  are respectively the dynamic viscosity, and thermal diffusivity of nitrogen, and a unity-Lewis-number assumption has been invoked.

Following the general procedure of OpenFOAM<sup>®</sup>-based codes, the governing equations are solved with a collocated finite-volume-method solver. This solver is transient, pressure-based and can handle unstructured meshes. With this approach, an inner iterative loop is used to correct the velocity field using the output of a pressure equation, as in the well-known PISO algorithm [44]. From recent findings [45], OpenFOAM<sup>®</sup>'s correction term for the mass fluxes in the PISO algorithm is not used here. The effect of this term was found to be negligible in simulations of the syngas flames discussed in this work. The models described here were incorporated within OpenFOAM<sup>®</sup> version 2.3.x, and they can, in principle, be used in conjunction with any combination of the various temporal and spatial discretization schemes available within OpenFOAM<sup>®</sup>.

### 3. Validation results

#### 3.1. Laminar, premixed flame

The present flame code was first used to model a laminar, one-dimensional, premixed, methane–air flame in order to compute the laminar flame speeds at various equivalence ratios. In contrast to commonly-used codes used for this purpose [46,47], the code framework used in the present work uses a time-marching algorithm. Thus, while traditional methods calculate the laminar flame speed  $S_L$  as an eigen value of the problem, the flame speed

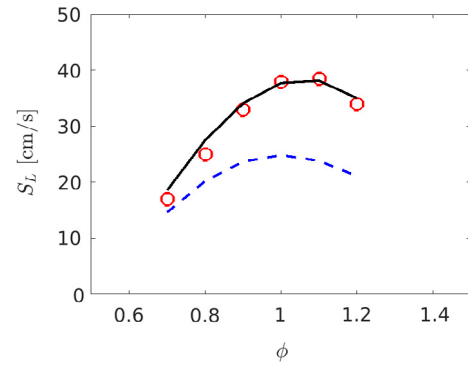


**Fig. 1.** Laminar burning velocity as a function of equivalence ratio for the methane–air flame. Red circles: experiments [49,50]; solid black line: using the mixture-averaged formulation; dashed blue line: using unity Lewis number for all species.

was obtained in this work by post-processing the solution data. A laminar burning velocity may be obtained as

$$S_L = -\frac{1}{\rho_1 Y_{F,1}} \int_{-\infty}^{\infty} \dot{\omega}_F dx, \quad (16)$$

where  $\rho_1$  is the density of the unburnt mixture,  $Y_{F,1}$  is the mass fraction of fuel in the unburnt mixture, and  $\dot{\omega}_F$  is the production rate of the fuel. The minus sign is used because the production rate of the fuel is negative.

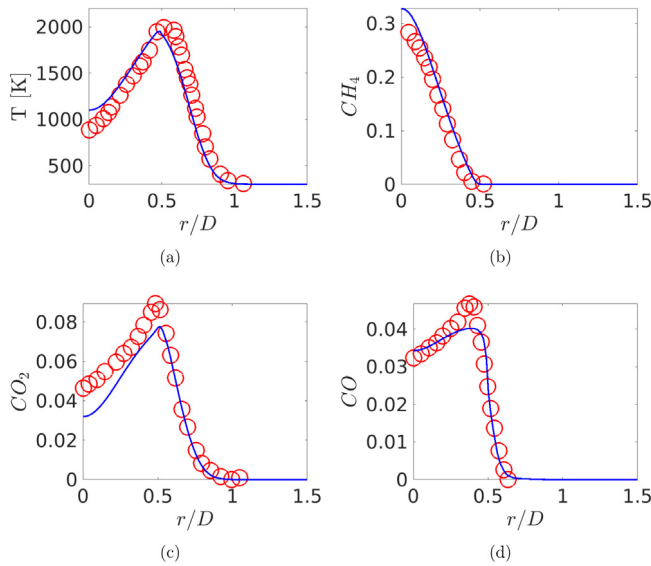
In this problem, the flame propagates inside a one-dimensional tube of length 40 mm that is divided into 1000 uniform hexahedral control volumes. At the inlet, the composition is held fixed at that of the corresponding reacting mixture at 300 K and 1 bar, whereas at the outlet zero-gradient boundary conditions are used in order to allow the products of combustion to freely leave the domain. The simulation is started from an initially quiescent flow field, and combustion is initialized by introducing high-temperature products within the domain. The low-Mach-number formulation was used for these simulations with a first-order time advancement scheme, a second-order, TVD-conforming scheme for the advective terms, and a second-order, central scheme for the diffusion terms. A time step of  $\Delta t = 1 \times 10^{-6}$  s was used in these simulations. A 16-step kinetic mechanism for methane oxidation [48] was used.

Fig. 1 shows flame-propagation-speed predictions and compares them with experimental data. It may be noted that the method used to calculate the transport properties has a strong influence on the results: the correct trend is predicted in either case, but the mixture-averaged transport model produces values which are closer to experimental values, especially at higher equivalence ratios.

#### 3.2. Laminar, non-premixed flame

The present code was also used to model a co-flowing laminar methane–air flame in the classical Burke and Schumann configuration [10,51–53]. The fuel flows through a central tube of diameter 12.7 mm, and the outer co-flow of air has a diameter of 50.8 mm. The burner is enclosed by a Pyrex glass cylinder, and so the outer boundary in the radial direction is modeled as a no-slip wall. The flow rates of the fuel and air are 5.7 cc/s and 187.7 cc/s respectively, which correspond to an inlet velocity of 4.5 cm/s for the fuel, and a co-flow velocity of 9.88 cm/s [10,53].

The computational domain started just downstream of the burner, and extended to a distance of 300 mm in the axial direction and 25.4 mm in the radial direction. Since the problem is known to be two-dimensional axi-symmetric, a 4° wedge was used instead



**Fig. 2.** Radial profiles of temperature and major gas-phase species for the laminar, co-flowing methane-air flame at a height of 12 mm from the burner. (○: experiments [52]; Solid line: present work.)

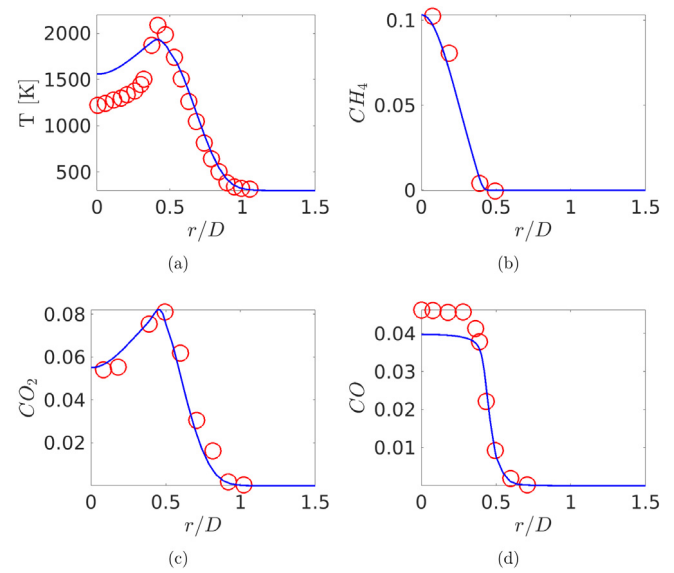


**Fig. 3.** Radial profiles of temperature and major gas-phase species for the co-flowing methane-air flame at a height of 24 mm from the burner. (○: experiments [52]; Solid line: present work.)

of the full cylinder. The domain was divided into  $171 \times 60$  non-uniform control volumes. The same 16-species gas-phase mechanism [48] of Section 3.1 was used. The flame preheating effect was ignored, as was the presence of the fuel tube wall. Uniform velocity profiles were prescribed for the fuel and air inflow, and an inlet temperature of 300 K was specified. Radiation was modeled by an optically-thin radiation model [43,54,55] using available OpenFOAM® libraries. Gravity was included in the axial component of the momentum equation as the body force,  $f_i$ . The low Mach number formulation was used, and the solution was marched in time from a carefully designed initial condition to speed up convergence. The advective terms in the momentum equation were discretized using a second-order central scheme, while for scalars a TVD-conforming, second-order scheme was used. The diffusion terms were discretized using a second-order central scheme.

Figs. 2 and 3 show the predicted temperature and major species profiles at two different heights from the burner. The agreement with experiment is generally good, particularly in view of the fact that experimental uncertainties are not available, and that the flame preheating effect was not accounted for. Also, this flame was experimentally determined to be a luminous flame, which means some soot is present in the flame. Radiation from soot can have a significant effect on the temperature field for such a flame [43], but since soot was not considered in the simulation, this introduces some additional uncertainty in the results.

These results are consistent with those obtained in previous studies of sooting and non-sooting laminar flames using earlier versions of this code [43,56–59]. Next, the code is assessed for a more challenging problem: turbulent flames undergoing extinction and reignition.

### 3.3. Turbulent, non-premixed flames

The next tests consider a reacting, temporally-evolving, planar jet in a cuboid of size  $L_x \times L_y \times L_z$  [60], as shown in Fig. 4. The fuel stream is an initially planar jet moving in the  $x$ -direction, while the oxidizer moves in the opposite direction on either side of the fuel stream. Turbulence is generated by shear at the interface between the two jets. In order to speed up the generation of shear-generated turbulence isotropic, broadband velocity fluctuations

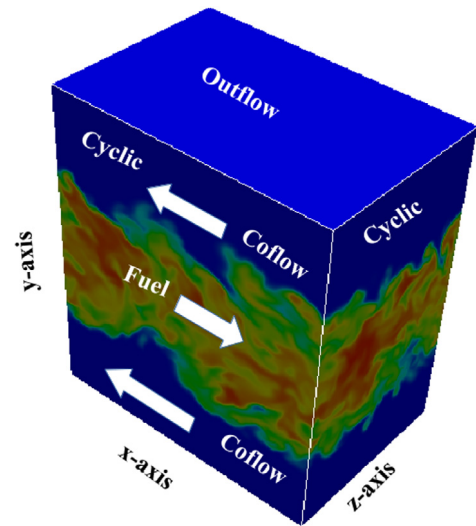


**Fig. 4.** Schematic of the DNS study configuration of Hawkes et al. [60]. Here temperature contours at  $t = 40 t_j$  are shown for the case M ( $Re = 4478$ ).

with a turbulence intensity of about 5% were imposed within the central fuel jet.

The fuel is syngas, comprising 50% CO, 10% H<sub>2</sub>, and 40% N<sub>2</sub> by volume. The oxidizer is composed of 25% O<sub>2</sub> and 75% N<sub>2</sub> by volume. Both fuel and oxidizer are initially at 500 K and react according to a skeletal mechanism for C<sub>1</sub>-kinetics [60]. The pressure is atmospheric. The characteristic jet velocity is  $U$ , and at  $t = 0$  both streams have a velocity of  $\frac{U}{2}$  in their respective directions. A characteristic length scale of the problem is the jet height  $H$ , and a characteristic jet time scale is  $t_j = \frac{H}{U}$ . Thus, a Reynolds number can be defined as  $Re = \frac{UH}{\nu_f}$ , where  $\nu_f$  is the kinematic viscosity of the pure fuel. The Damköhler number is defined as  $Da = \chi_q t_j$ , with  $\chi_q$  being the quenching scalar dissipation rate for the flamelet solution that was used to initialize the combustion.

By changing  $H$  and  $U$ , the DNS study [60] varied  $Re$  while keeping  $Da$  constant to produce the three cases shown in Table 1: the low- $Re$  case L, the medium- $Re$  case M, and the high- $Re$  case



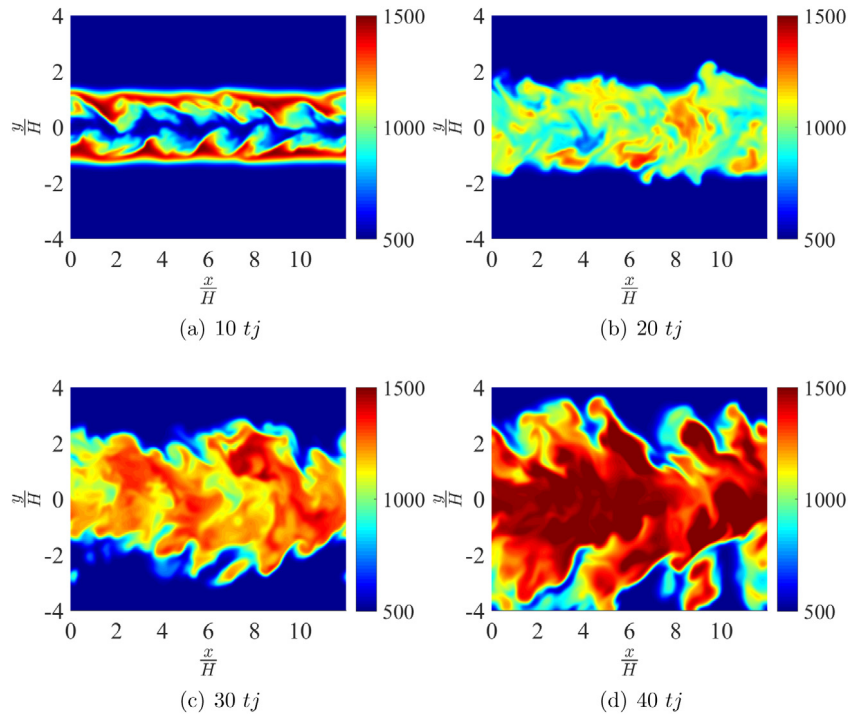


**Fig. 5.** Instantaneous temperature contours at the center plane ( $z = 0$ ) for case M, on the finest mesh.

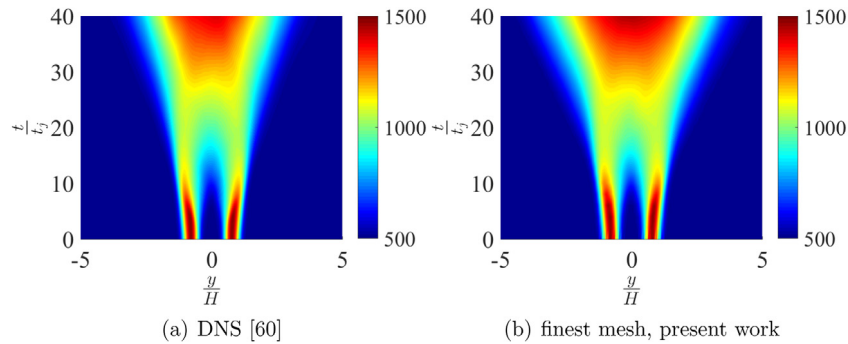


**Fig. 6.** Spatially averaged temperature fields for case M showing the extinction and reignition process.

**Table 1**  
Parameters used for the DNS study of Hawkes et al. [60].

Case	H (mm)	Re	$\Delta x (\mu\text{m})$	$\Delta x / \eta$	$t_j (\mu\text{s})$	$U (\text{ms}^{-1})$	Da	Ma
L	0.72	2510	15.0	0.8	4.88	147.36	0.011	0.16
M	0.96	4478	15.0	1.1	4.96	193.41	0.011	0.21
H	1.37	9079	19.0	1.67	4.96	276.30	0.011	0.3

H. The DNS was designed to attain values of  $Re$  and  $Da$  that would produce some extinction and reignition [60]. In each of these cases the size of the computational domain is given by  $L_x = 12H$ ,  $L_y = 14H$ , and  $L_z = 8H$ . The (global) Mach number is  $Ma = \frac{U}{c_1 + c_2}$ , where  $c_1 = 476 \text{ ms}^{-1}$ , and  $c_2 = 445 \text{ ms}^{-1}$  are the sound speeds in the fuel and oxidizer streams, respectively. Hawkes et al. used a fully compressible formulation along with a mixture-averaged method to calculate the transport properties, and the mesh resolution was chosen to adequately resolve all turbulent scales as well as the flame structure [60].

In the present work, simulations of the jets M and H were performed with the low-Mach-number formulation, unless said otherwise. The setup of the DNS was followed closely, except for the resolution of the uniform mesh: the present work used meshes

which were four and eight times coarser than the mesh used in the corresponding DNS study. The two meshes are hereafter referred to as the finest, and the fine mesh respectively. The simulations on the fine mesh were run on 48 cores, while those on the finest mesh were run on 96 processors. Their cost is indicated later.

A fixed time step of  $\Delta t = 0.2 \mu\text{s}$  was used for the simulations on the fine mesh, while the value was lowered by a factor of two for the finest mesh. These stepsizes correspond to a Courant number of  $\sim 0.25$  for the simulations. This value was obtained from a sensitivity study in order to find the optimal stepsize in terms of accuracy and computational cost. However it should be noted that the appropriate value of the Courant number is likely to be a problem-dependent parameter.

Another difference from the DNS was the treatment of the boundaries at the ends of the vertical extent of the domain. The DNS used a fully compressible formulation, and thus to eliminate acoustic waves, a non-reflecting outflow condition was used in the vertical ( $y$ ) direction. Since a low-Mach-number approximation was used in the present work, a fixed value of zero was prescribed for the dynamic pressure at the same boundaries, which corresponds to an atmospheric pressure condition. Homogeneous Neumann boundary conditions were used for all other quantities.

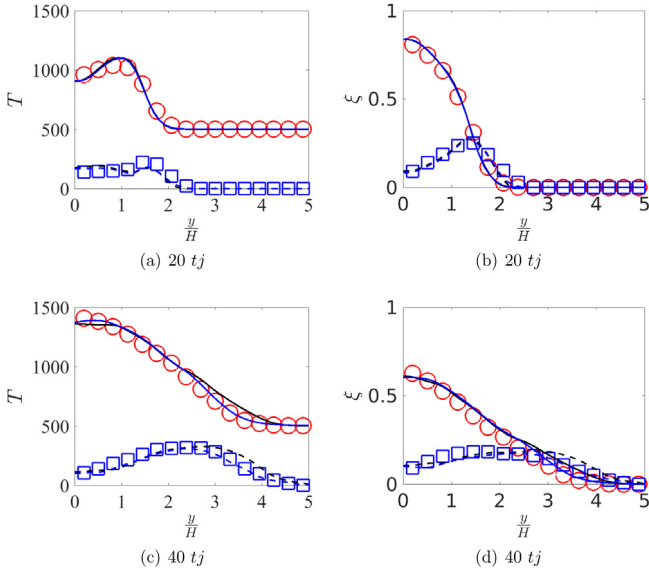


**Fig. 7.** Low-Mach-number versus fully-compressible formulation in case M on the fine mesh. (Black solid line: mean, low-Ma; blue solid line: mean, fully compressible;  $\circ$ : mean, DNS [60]; black dashed line: rms, low-Ma; blue dashed line: rms, fully compressible;  $\square$ : rms, DNS [60].)

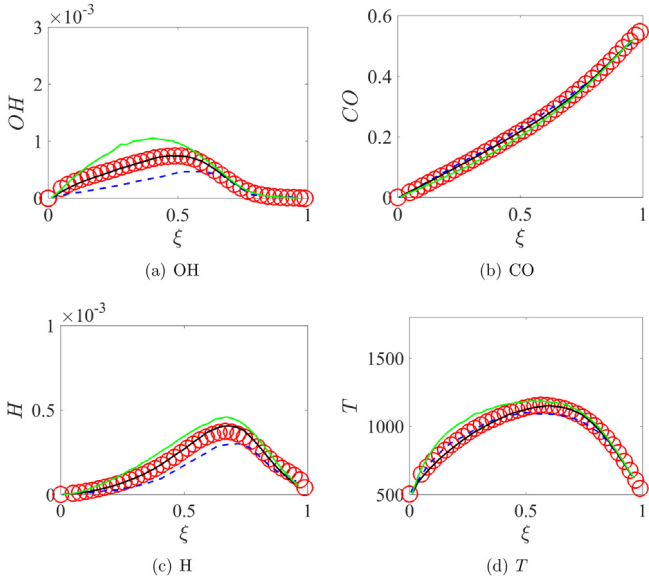


**Fig. 8.** Mixture fraction-conditioned profiles of temperature and species mass fractions at 20  $t_j$  for case M. (Black solid line: finest mesh; green solid line: fine mesh; blue dashed line: Sen et al. [61,62];  $\circ$ : DNS [60].)

Like the DNS, periodic boundary conditions were specified in the streamwise ( $x$ ) and the span-wise ( $z$ ) directions.

To start the calculation all scalars were initialized from planar-averaged (in the  $xz$  plane) DNS data, while the full three-dimensional velocity field was mapped onto the present meshes. Thus the same method of triggering the shear-generated turbulence by using isotropic velocity fluctuations within the fuel layer was used in the present work. A blended Crank–Nicolson scheme was used to advance the solution in time. The advective terms in the momentum equation were discretized by a second-order linear scheme, while a TVD-conforming, second-order scheme was used to advect the scalars. Diffusion terms were discretized by a second order central difference scheme.

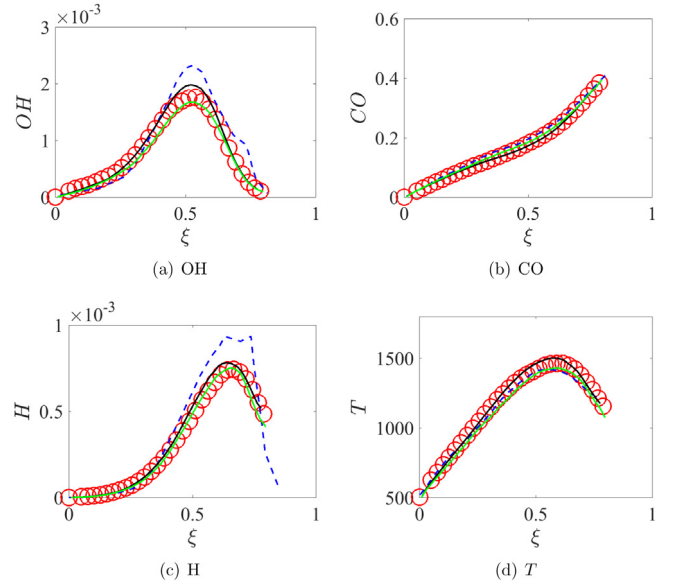


**Fig. 9.** Mixture fraction-conditioned profiles of temperature and species mass fractions at 40  $t_j$  for case M. (Black solid line: finest mesh; green solid line: fine mesh; blue dashed line: Sen et al. [61,62];  $\circ$ : DNS [60].)

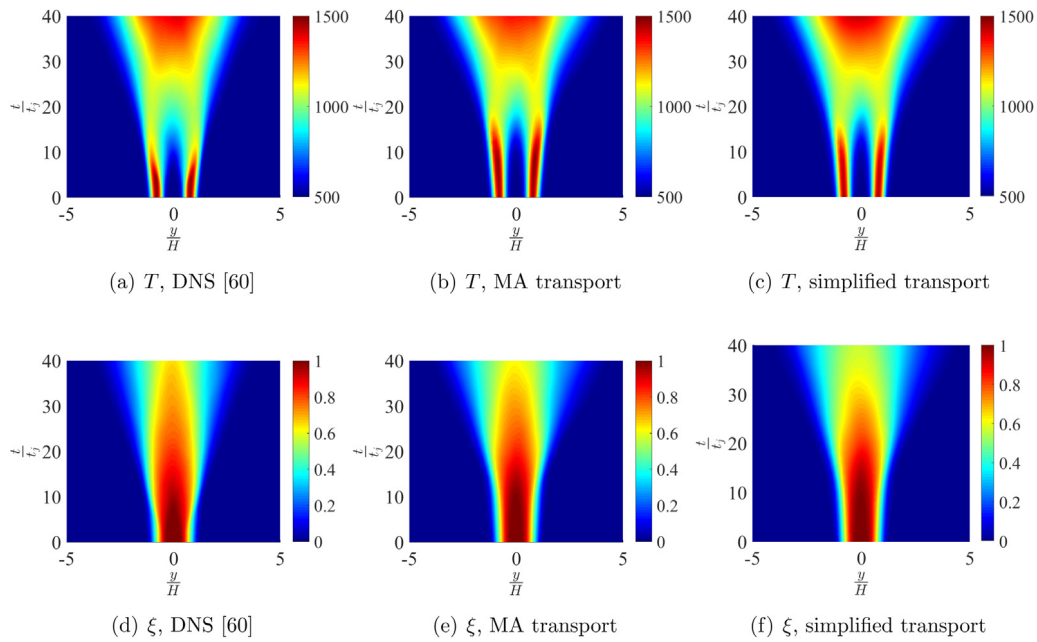
The present code framework may be used in conjunction with SGS closure models such as the Smagorinsky model [63]. However, at the spatial resolutions used in the present simulations, the contribution from the subgrid turbulence closure model was found to be negligible. Hence the simulations reported in this work used no subgrid closure models, and may be thought of as an implicit LES, where the numerical dissipation mimics subgrid transport.

### 3.3.1. Case M

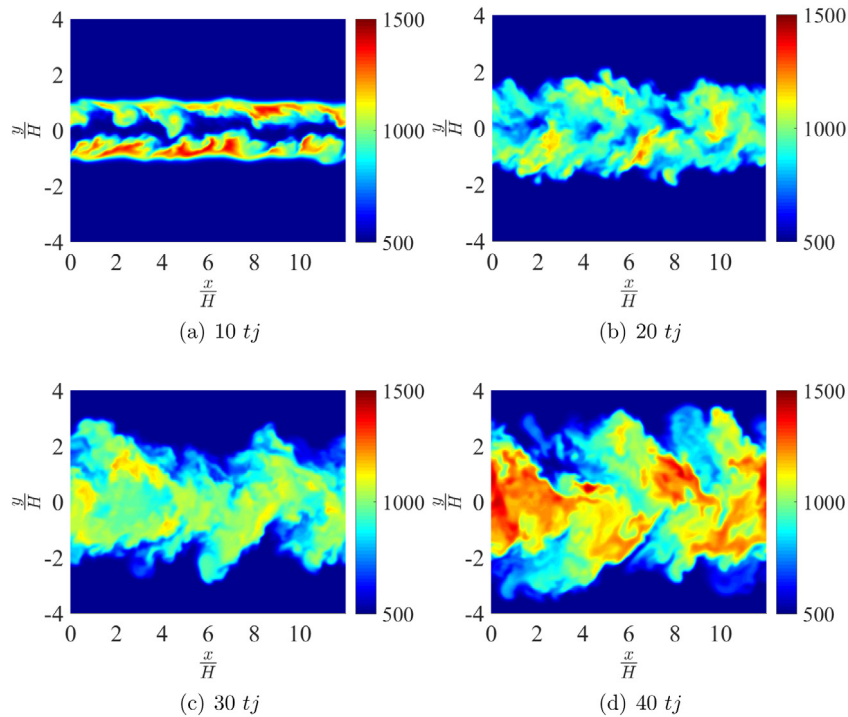
Case M has a Reynolds number of 4478. The DNS study of this jet was conducted on a mesh of size  $768 \times 896 \times 512$ , while the meshes used in the present work were of size  $192 \times 224 \times 128$ , and  $96 \times 112 \times 64$ , producing mesh spacings of  $60 \mu\text{m}$  and  $120 \mu\text{m}$  respectively.

Fig. 5 shows the temperature contours on the center ( $z = 0$ ) plane at different times in the flow evolution on the finest mesh. It is seen that the two initial high-temperature regions of Fig. 5(a) are later broken up by shear-driven vortices. Also the mixing layer, seen here as a high-temperature region, grows as these vortices develop. Fig. 5 also shows that the overall temperature initially decreases and later increases. These two processes are termed extinction and reignition respectively, as was done previously [60].

To compare present predictions with DNS, quantities are spatially averaged in the  $xz$  plane to obtain means and root-mean-squared (rms) values. From now on, the term accuracy refers to the difference between present results and DNS. Fig. 6 shows for case M the temporal evolution of these mean values for temperature. As discussed above for Fig. 5, notice in Fig. 6 that as time progresses the mean temperature decreases and then increases, while the mixing-layer width grows. It is also interesting to notice in Fig. 6 that, by visualizing the temporal axis as the centerline axis of a spatially-developing jet, the present reacting jet can be said to exhibit lift-off. More importantly for the present purposes, Fig. 6 shows that the agreement between present predictions and DNS data is good, perhaps except near the end of the simulation where present simulations give a broader mixing layer. Nonetheless, it must be kept in mind that capturing extinction–reignition is difficult [64]. Thus, to better assess the accuracy of the present code, a comparison is made later between present predictions and those from a simulation that does not use a DNS mesh resolution.



**Fig. 10.** Spatially averaged temperature and mixture fraction ( $\xi$ ) fields for case M on the fine mesh showing the extinction and reignition process. MA denotes mixture-averaged transport.



**Fig. 11.** Instantaneous temperature contours at the center plane ( $z = 0$ ) for case H, on the finest mesh.

For both low-Mach-number and fully-compressible simulations with the fine mesh, Fig. 7 shows the spatially-averaged temperature and mixture fraction profiles at two instants during the simulation. Hawkes et al. [60] report that  $20 t_j$  corresponds roughly to the point of maximum extinction, and by  $40 t_j$  the reignition is significant. Thus, these two times present suitable comparison points. Fig. 7 indicates that both formulations are able to capture the extinction and reignition of the DNS. Moreover, Fig. 7 shows that predictions from both formulations are close to each other. In

view of this result, and considering that simulations with the low-Mach-number (fully-compressible) formulation take 64 (1200) CPU-hours, only results from low-Mach-number simulations are discussed from now on.

Figs. 8 and 9 compare the results in mixture fraction space obtained in the present work with those reported by Sen and Menon [61,62]. The DNS data is also included. Sen and Menon use a fully-compressible formulation, a one-equation SGS momentum transport model, a linear-eddy model of turbulent combustion [65, 66], and a non-uniform mesh with spacings ranging from 35 to



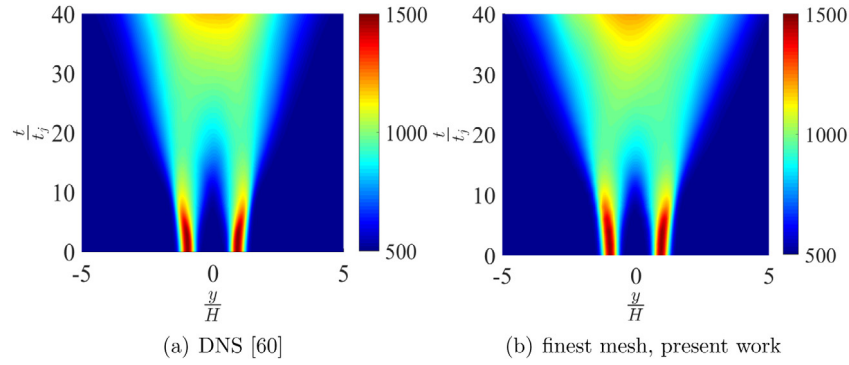


Fig. 12. Spatially averaged temperature fields for case H showing the extinction and reignition process.

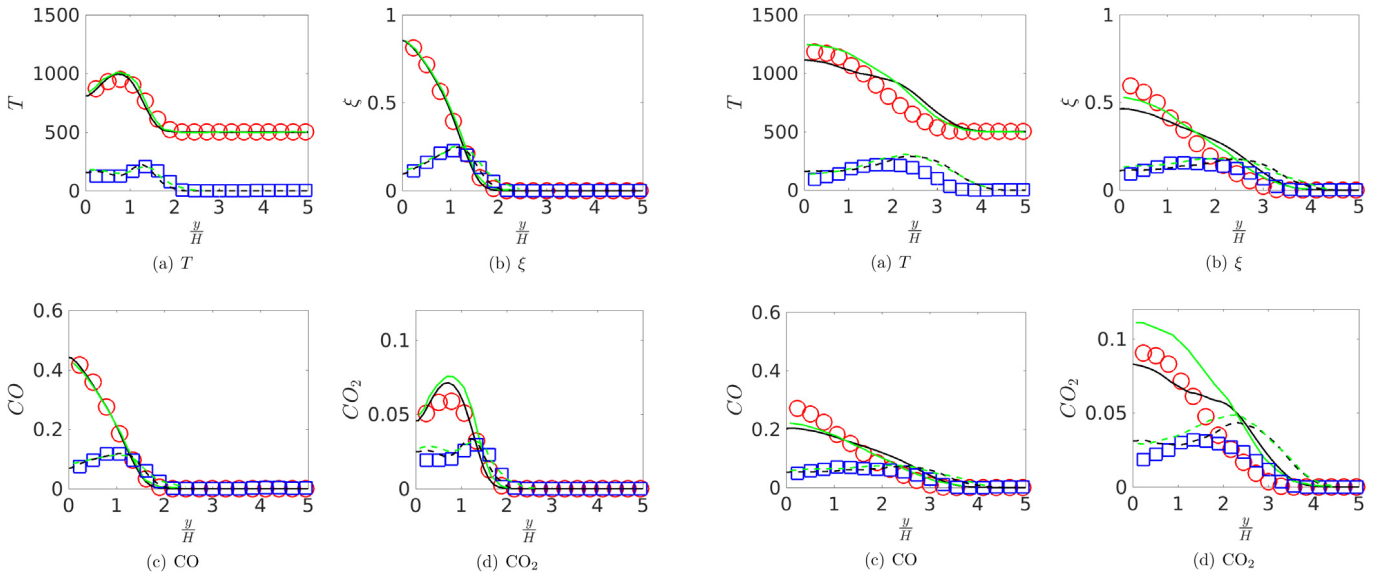


Fig. 13. Mean and rms profiles for case H at  $20 t_j$  from the fine mesh, compared with Yang et al. [68]. (Black solid line: mean, fine mesh; green solid line: mean, Yang et al. [68]; black dashed line: rms, fine mesh; green dashed line: rms, Yang et al. [68]; o: mean, DNS [60]; □: rms, DNS [60].)

Fig. 14. Mean and rms profiles for case H at  $40 t_j$  from the fine mesh, compared with Yang et al. [68]. (Black solid line: mean, fine mesh; green solid line: mean, Yang et al. [68]; black dashed line: rms, fine mesh; green dashed line: rms, Yang et al. [68]; o: mean, DNS [60]; □: rms, DNS [60].)

125  $\mu\text{m}$ . In contrast, the present work uses no explicit turbulent transport or combustion models, and relatively coarser, uniform mesh spacings of 60 and 120  $\mu\text{m}$ . It is seen that present agreement with the DNS data is as good as those reported by Sen and Menon.

It is also important to note from Figs. 8 and 9 that the effect of using the fine or finest mesh is small, except for OH predictions. This result suggests that numerical errors are not dominant. Therefore, the good accuracy from the present code is not fortuitous.

Fig. 10 compares predictions of the spatially-averaged temperature and mixture fraction from the current mixture-averaged molecular transport with those from OpenFOAM®'s simplified molecular-transport approach. For the latter, a low-Mach-number version of reactingFoam is used [67], which uses Eqs. (1)–(3) and (7)–(8). It is seen in Fig. 10 that the use of the current mixture-averaged molecular transport does provide an enhancement of accuracy, in particular in the mixture fraction map. This is achieved with a computational cost 20% higher than with the simplified molecular transport.

### 3.3.2. Case H

Case H has a Reynolds number of 9079. The DNS of this jet used a mesh of size  $864 \times 1008 \times 576$ , while the present work used meshes of size  $216 \times 252 \times 144$ , and  $108 \times 126 \times 72$ . The mesh

spacings for the fine and the finest meshes used in the present work are therefore 152 and 76  $\mu\text{m}$  respectively. The computational cost for a low-Mach-number simulation on the fine mesh is about 113 CPU hours, while that cost rises to 2137 CPU hours for the finest mesh.

Fig. 11 shows the temperature contours at the center ( $z = 0$ ) plane on the finest mesh at different times in the simulation. As in case M (Section 3.3.1), the extinction–reignition process is captured by the present code. In particular, it is seen in Fig. 11(b) that at  $20 t_j$  the flame undergoes significant extinction. This is followed by a subsequent reignition, as Figs. 11(c) and 11(d) show. It is seen that the minimum temperatures are lower in case H in comparison to case M. This can be seen as surprising since  $Da$  is the same in cases M and H. Nonetheless, these lower temperatures may also be due to higher intermittency at the higher  $Re$  of Case H [60], which can lead to higher dissipation rates and thus a more pronounced extinction [69]. (Further analysis of the DNS data could clarify this effect, but this analysis is considered outside the scope of the present work.) Another difference between cases M and H is that at the end of the reignition the temperatures are higher in case M. This result is likely due to the fact that case H has not been run long enough for a full reignition [60].

Fig. 12 shows the spatially-averaged temperature fields in  $y - t$  coordinates predicted from present simulations and the DNS. The

agreement with the DNS is seen to be fairly good, both in terms of the vertical ( $y$ -directional) spread of the reacting zone, and the time scales involved. However, as in case M, there is some discrepancy near the end of the simulation, where present predictions give more mixing. This discrepancy is also seen in another study [68]. To better assess a comparison of present predictions with DNS data, a comparison with previous simulations using a mesh coarser than the DNS is discussed next.

Figs. 13 and 14 compare present predictions using the fine mesh to those of Yang et al. [68]. The DNS data is also included. Yang et al. used the NGA code [70] with a low-Mach-number formulation, a dynamic SGS momentum transport model [71], a transported PDF method, and a uniform mesh spacing of 152  $\mu\text{m}$ . The same mesh resolution was used in the present work. However, present simulations used no explicit SGS models. Overall, Figs. 13 and 14 show that the current simulation can produce results that are as accurate as those from Yang et al.

#### 4. Conclusion

The present work discusses and tests a new OpenFOAM®-based code whose key feature is its capability to account for molecular transport using a detailed, mixture-averaged computation of transport coefficients. The code predicts with good accuracy the flame speed for a laminar, one-dimensional, premixed flame. Moreover, present predictions for temperature and species profiles for a laminar, two-dimensional, non-premixed flame where radiation is non-negligible are in good agreement with experimental data. In addition, the code predictions for the mean and rms temperature and species mass fractions agree well with DNS data in the non-trivial problem of extinction-reignition in two turbulent, three-dimensional, non-premixed flames. Such an agreement is within that of two previous studies using state-of-the-art flame codes. In the premixed-flame and turbulent-flame problems, the present detailed-transport model is more accurate than a simplified model. Overall, the present flame code provides predictions which are in good agreement with experimental and DNS data. Hence, considering that the present code is readily available [29], and noticing the insight into combustion physics and combustor design that combustion codes have provided, the present code has the potential to expand the community of people providing this type of insight. Future work should include modeling of premixed or partially-premixed turbulent flames, the consideration of real fluids as opposed to ideal gases, and the capability to model high-pressure, and high-speed reacting flows.

#### Acknowledgments

The authors would like to thank Prof. Evatt Hawkes for kindly providing the syngas DNS data used in the present study. This work was conducted thanks to the financial support from The Pennsylvania State University and Combustion Science & Engineering, Inc.

#### References

- [1] J.H. Chen, *Proc. Combust. Inst.* 33 (1) (2011) 99–123.
- [2] C.J. Rutland, *Int. J. Engine Res.* 12 (5) (2011) 421–451.
- [3] L.Y.M. Gicquel, G. Staffelbach, T. Poinsot, *Prog. Energy Combust. Sci.* 38 (6) (2012) 782–817.
- [4] ANSYS, *Fluent Theory Guide*, ANSYS, 2011.
- [5] STARCCM+ User Guide, CD-Adapco, 2011.
- [6] The National Combustion Code, 2018, [flight.nasa.gov/events/home&home/glenn/simula1/sld004.htm](https://flight.nasa.gov/events/home&home/glenn/simula1/sld004.htm).
- [7] VULCAN, 2018, <https://vulcan-cfd.larc.nasa.gov>.
- [8] J.H. Chen, A. Choudhary, B. de Supinski, M. DeVries, E.R. Hawkes, S. Klasky, W.K. Liao, K.L. Ma, J. Mellor-Crummey, N. Podhorszki, R. Sankaran, S. Shende, C.S. Yoo, *Comput. Sci. Discov.* 2 (1) (2009) 015001.
- [9] AVBP, 2018, [www.cerfacs.fr/avbp7x](http://www.cerfacs.fr/avbp7x).
- [10] W. Roquemore, V. Katta, *J. Vis.* 2 (3–4) (2000) 257–272.
- [11] H. Guo, F. Liu, G.J. Smallwood, O.L. Gülder, *Combust. Theory Model.* 6 (2002) 173–187.
- [12] OpenFOAM, 2018, <http://www.openfoam.org>.
- [13] H.G. Weller, G. Tabor, H. Jasak, C. Fureby, *Comput. Phys.* 12 (6) (1998) 620–631.
- [14] A. Fancello, L. Panek, O. Lammel, W. Krebs, R.J.M. Bastians, L.P.H. de Goey, *Proceedings of ASME Turbo Expo 2014: Turbine Technical Conference and Exposition GT 2014*, 2014.
- [15] G.M. Ottino, A. Fancello, M. Falcone, R.J.M. Bastiaans, L.P.H. de Goey, *Flow Turbul. Combust.* 96 (3) (2016) 773–800.
- [16] C. Fureby, *Philos. Trans. R. Soc. Lond. Ser. A Math. Phys. Eng. Sci.* 367 (1899) (2009) 2957–2969.
- [17] M. Chapuis, C. Fureby, E. Fedina, N. Alin, J. Tegnér, *ECCOMAS CFD*, 2010.
- [18] Y. Wang, P. Chatterjee, J.L. de Ris, *Proc. Combust. Inst.* 33 (2) (2011) 2473–2480.
- [19] C. Gong, M. Jangi, X. Bai, *Appl. Energy* 136 (2014) 373–381.
- [20] B. Fiorina, R. Mercier, G. Kuenne, A. Ketelheun, A. Avdić, J. Janicka, D. Geyer, A. Dreizler, E. Alenius, C. Duwig, et al., *Combust. Flame* 162 (11) (2015) 4264–4282.
- [21] Z. Huang, G. He, F. Qin, X. Wei, *Int. J. Hydrogen Energy* 40 (31) (2015) 9815–9824.
- [22] E.D. Gonzalez-Juez, *AIAA Paper* 2015-3965, 2015.
- [23] E.D. Gonzalez-Juez, *AIAA Paper* 2017-4686, 2017.
- [24] J. van Oijen, L. De Goey, *Combust. Sci. Technol.* 161 (1) (2000) 113–137.
- [25] J. Van Oijen, F. Lammers, L. De Goey, *Combust. Flame* 127 (3) (2001) 2124–2134.
- [26] J.A. Van Oijen, L.P.H. De Goey, *Combust. Theory Model.* 6 (3) (2002) 463–478.
- [27] A. Cuoci, A. Frassoldati, T. Faravelli, E. Ranzi, *Combust. Flame* 160 (2013) 870–886.
- [28] F. Zhang, H. Bonart, T. Zirwes, P. Habisreuther, H. Bockhorn, N. Zarzal, in: W.E. Nagel, D.H. Kröner, M.M. Resch (Eds.), *High Performance Computing in Science and Engineering '14*, Springer International Publishing, Cham, 2015, pp. 221–236.
- [29] Adhiraj Dasgupta's Code, 2018, <https://github.com/adhiraj-dasgupta/unsupportedContribOF23x>.
- [30] D. Lignell, J. Chen, H. Schmutz, *Combust. Flame* 158 (5) (2011) 949–963.
- [31] A.G. Tomboulides, J.C.Y. Lee, S.A. Orszag, *J. Sci. Comput.* 12 (2) (1997) 139–167.
- [32] B.J. McBride, S. Gordon, M.A. Reno, *Coefficients for Calculating Thermodynamic and Transport Properties of Individual Species*, NASA, 1993.
- [33] G. Bader, P. Deufhard, *Numer. Math.* 41 (3) (1983) 373–398.
- [34] J.O. Hirschfelder, C.F. Curtiss, R.B. Bird, *Molecular Theory of Gases and Liquids*, John Wiley & Sons, New York, 1994.
- [35] R.J. Kee, G. Dixon-Lewis, J. Warnatz, M.E. Coltrin, J.A. Miller, *A Fortran Computer Code Package for the Evaluation of Gas Phase Multicomponent Transport Properties*, Sandia National Laboratory, 1986.
- [36] T. Coffee, J. Heimerl, *Combust. Flame* 43 (1981) 273–289.
- [37] P.D. Neufeld, A.R. Janzen, A.R. Aziz, *J. Chem. Phys.* 57 (1972) 1100–1102.
- [38] N. Peters, J. Warnatz (Eds.), *Numerical Methods in Laminar Flame Propagation*, Vieweg & Teubner Verlag, 1982.
- [39] R.B. Bird, W.E. Stewart, E.N. Lightfoot, *Transport Phenomena*, John Wiley and Sons, Inc., New York, 1960.
- [40] C.R. Wilke, *J. Chem. Phys.* 18 (4) (1950) 517–519.
- [41] S. Mathur, P. Tondon, S. Saxena, *Mol. Phys.* 12 (1967) 569–579.
- [42] B. Gough, *GNU Scientific Library Reference Manual*, third ed., Network Theory Ltd., 2009.
- [43] A. Dasgupta, *Numerical Simulation of Axisymmetric Laminar Diffusion Flames with Soot* (Ph.D. thesis), Pennsylvania State University, 2015.
- [44] R.I. Issa, *J. Comput. Phys.* 62 (1) (1986) 40–65.
- [45] V. Vuorinen, J.P. Keskinen, C. Duwig, B. Boersma, *Comput. & Fluids* 93 (2014) 153–163.
- [46] R.J. Kee, J.F. Grcar, M.D. Smooke, J.A. Miller, *Technical Report SAND85-8240*, Sandia National Laboratories, 1985.
- [47] D.G. Goodwin, H.K. Moffat, R.L. Speth, *Cantera: An Object-oriented Software Toolkit for Chemical Kinetics, Thermodynamics, and Transport Processes*, Version 2.3.0, 2017.
- [48] S. James, M.S. Anand, M.K. Razdan, S.B. Pope, *J. Eng. Gas Turbines Power* 123 (2001) 747–756.
- [49] C. Vagelopoulos, F. Egolfopoulos, *Twenty-Fifth Symposium (International) on Combustion, Symp. (Intl.) Combust.* 25 (1) (1994) 1317–1323.
- [50] I. Glassman (Ed.), *Combustion*, third ed., Academic Press, San Diego, 1996, pp. 575–580.
- [51] S.P. Burke, T.E.W. Schumann, *Ind. Eng. Chem.* 20 (10) (1928) 998–1004.
- [52] R.E. Mitchell, A.F. Sarofim, L.A. Clomberg, *Combust. Flame* 37 (1980) 227–244.
- [53] M.D. Smooke, R.E. Mitchell, D.E. Keyes, *Combust. Sci. Technol.* 67 (1989) 85–122.
- [54] H. Guo, F. Liu, G.J. Smallwood, *Combust. Theory Model.* 8 (1991) 475–489.
- [55] R.S. Barlow, A.N. Karpetis, J.H. Frank, J.Y. Chen, *Combust. Flame* 127 (2001) 2102–2118.
- [56] A. Dasgupta, S. Roy, D.C. Haworth, *Proceedings of the 2014 Annual Conference on Extreme Science and Engineering Discovery Environment, XSEDE '14*, ACM, New York, NY, USA, 2014, pp. 12:1–12:7.

- [57] J. Cai, S. Lei, M.F. Modest, A. Dasgupta, D.C. Haworth, Proceedings of the ASME 2012 International Mechanical Engineering Congress & Exposition, 2012.
- [58] S. Lei, J. Cai, M.F. Modest, A. Dasgupta, D.C. Haworth, Proceedings of the ASME 2012 International Mechanical Engineering Congress & Exposition, 2012.
- [59] J. Cai, S. Lei, A. Dasgupta, M.F. Modest, D.C. Haworth, *Combust. Theory Model.* 18 (6) (2014) 607–626.
- [60] E.R. Hawkes, R. Sankaran, J.C. Sutherland, J.H. Chen, Proceedings of the combustion institute 31 (1) (2007) 1633–1640.
- [61] B.A. Sen, Artificial Neural Networks based Subgrid Chemistry Model for Turbulent Reactive Flow simulations (Ph.D. thesis, ), Georgia Institute of Technology, 2009.
- [62] B.A. Sen, S. Menon, *Combust. Flame* 157 (1) (2010) 62–74.
- [63] J. Smagorinsky, *Mon. Weather Rev.* 91 (3) (1963) 99–164.
- [64] D.O. Lignell, D.S. Rappleye, *Combust. Flame* 159 (9) (2012) 2930–2943.
- [65] A.R. Kerstein, *Combust. Sci. Technol.* 60 (4–6) (1988) 391–421.
- [66] S. Menon, A.R. Kerstein, *Turbulent Combust. Model.* (2011) 221–247.
- [67] K.J. Nogenmyr, C. Chan, C. Duwig, 5th OpenFOAM Workshop, Chalmers, Gothenburg, Sweden, 2010.
- [68] Y. Yang, H. Wang, S.B. Pope, J.H. Chen, *Proc. Combust. Inst.* 34 (1) (2013) 1241–1249.
- [69] J.C. Hewson, A.R. Kerstein, *Combust. Sci. Technol.* 174 (5–6) (2002) 35–66.
- [70] O. Desjardins, G. Blanquart, G. Balarac, H. Pitsch, *J. Comput. Phys.* 227 (15) (2008) 7125–7159.
- [71] C.D. Pierce, P. Moin, *J. Fluid Mech.* 504 (1) (2004) 73–97.